Magnetic field effects on three-dimensional natural convection

S. RENAUDIÈRE DE VAUX[a, b], R. ZAMANSKY[a], W. BERGEZ[a], P. TORDJEMAN[a], V. BOUYER[b], P. PILUSO[b], J.F. HAQUET[b]

a. Université de Toulouse, INPT-CNRS, Institut de Mécanique des Fluides de Toulouse,
1 Allée du Professeur Camille Soula, 31400 Toulouse, France.
srenaudi@imft.fr
b. CEA, DEN, Cadarache, SMTA/LPMA, F13108 St Paul lez Durance, France.

Résumé :

Nous étudions l'influence du champ magnétique sur la structure d'un écoulement de convection thermique. Le champ magnétique modifie le flux de chaleur à la paroi. Il tend à détruire les motifs tridimensionnels et à rendre l'écoulement bidimensionnel. La dernière partie présente une extension de l'analyse de stabilité marginale à l'aide d'un schéma aux différences finies. Nous présentons également la validation des développements au sein du code volumes finis Jadim grâce à la simulation numérique d'écoulements magnétohydrodynamiques (MHD) possédant des solutions analytiques.

Abstract:

This paper provides a validation of a finite volume code through the simulation of two configurations that can be solved analytically. We study the structure of a magnetoconvective flow. The magnetic field modifies the heat fluxes at the walls. It tends to destroy the three-dimensional patterns in favor of two-dimensional rolls. The last part of this paper consists in an extent to the marginal stability theory, thanks to a finite difference scheme. We also present the validation of the developments of the finite volume code Jadim, thanks to the simulation of magnetohydrodynamic (MHD) flows that have analytical solutions.

Mots clefs : computational fluid dynamics, magnetoconvection, heat transfer, linear stability

1 Introduction

Our study aims at simulating the molten corium behaviour in the presence of an AC magnetic field. The purpose of induction heating at CEA (Commissariat à l'Energie Atomique) is to heat the bulk of the fluid, in order to mimic the residual power of nuclear disintegrations that occur in the case of a severe nuclear accident. The question is then how the Lorentz force modifies the flow structure. To adress this issue, we propose to model this case through a Rayleigh-Bénard configuration, that will allow us to study the thermonconvective mechanisms in the presence of an AC magnetic field.

This case consists in a fluid in a cavity heated from below and cooled from above. The Rayleigh-Bénard convection has been widely studied, and Chandrasekhar [1] theorised the onset of convection in hydromagnetics. Rayleigh-Bénard experiments have been carried out in a magnetic field and confirm Chandrasekhar's results that the magnetic field tends to stabilise the flow, since the Lorentz force is opposed to the velocity. Rossby [2], Aurnou and Olson [3] and Burr and Müller [4] studied the influence of a vertical magnetic field on the Rayleigh-Bénard convection in different fluids. They proposed empirical correlations linking the Rayleigh number to the Nusselt number without magnetic field, in thermoconvection (TC). Aurnou and Olson [3] proposed similar correlation in

magnetoconvection (MC) that takes into account the influence of the magnetic field. Burr and Müller [5] also studied the thermal convection in presence of a horizontal magnetic field. Those low-Prandtl experiments (typical for liquid metals) confirm the general Nusselt-Rayleigh correlation in TC from Globe and Dropkin [6] that also gives the dependance in Prandtl number.

In a first part, we will proceed to validate the CFD code Jadim, a research code developped at IMFT (Institut de Mécanique des Fluides de Toulouse) in magnetoconvection to simulate the Rayleigh-Bénard instability in a second part. The last part of this paper is an extension of Chandrasekhar's marginal stability theory. This last work will help us understand if the amplified wavelength is conserved after the apparition of non-linear effects, accessible through Jadim simulations. Also interesting are the eigenvectors at the onset of convection for the amplified wavenumber k_{max}, that provide the profiles of the velocity, temperature and magnetic field perturbations.

2 Validation of the Jadim code in magnetohydrodynamics

The Jadim code has been developped as a research tool for solving two-phase flow problems. This code solves the Navier-Stokes equations and the heat equation using a Runge-Kutta scheme and a Crank-Nicholson scheme for the implicit terms. A projection method is used for solving the pressure term. In this paper, we use a Boussinesq model $\beta = -\frac{1}{\rho_0}\frac{\partial \rho}{\partial T}$, in order to take into account the density variations and the buoyancy forces. We add a magnetic Lorentz force $\mathbf{j} \times \mathbf{B_0}$, assuming a constant and uniform magnetic field $\mathbf{B_0}$:

$$\frac{\mathrm{D}\mathbf{U}}{\mathrm{D}t} = -\nabla \frac{p}{\rho_0} + \beta(T - T_0)\mathbf{g} + \nu \triangle \mathbf{U} + \frac{1}{\rho_0}\mathbf{j} \times \mathbf{B_0}, \tag{1}$$

where $\mathbf{j} = \sigma \mathbf{U} \times \mathbf{B_0}$ is the current density, and the energy equation:

$$\frac{\mathrm{D}T}{\mathrm{D}t} = \kappa \triangle T + \frac{1}{\rho c_p}\frac{j^2}{\sigma}. \tag{2}$$

Here ν, κ, $\mathbf{g}$, σ are the kinematic viscosity, thermal diffusivity, acceleration of gravity and electrical conductivity. Simulations were done with computations of the Joule term and it appears to be of no significant interest. Scaling the flow with an advective time gives:

$$\frac{\partial \mathbf{u}^*}{\partial t^*} + (\mathbf{u}^* \cdot \nabla^*)\mathbf{u}^* = -\nabla p^* + \frac{1}{Re}\triangle^* \mathbf{u}^* - \frac{Ra}{Re^2 Pr} T^* \mathbf{e_z} + \frac{Ha^2}{Re}\mathbf{j}^* \times \mathbf{B}^*, \tag{3}$$

$$\frac{\partial T^*}{\partial t^*} + (\mathbf{u}^* \cdot \nabla^*)\mathbf{T}^* = \frac{1}{RePr}\triangle^* T^*, \tag{4}$$

where $Re = \frac{u_0 e}{\nu}$, $Pr = \frac{\nu}{\kappa}$, $Ra = \frac{g\beta\Delta T e^3}{\nu\kappa}$, $Ha = B_0 e\sqrt{\frac{\sigma}{\rho\nu}}$ respectively are the Reynolds, Prandtl, Rayleigh and Hartmann numbers, and the variables X^* denote the dimensionless variables. Here ΔT is the imposed temperature difference and e is the gap between the horizontal plates.

If we estimate the typical velocity u_0 thanks to the buoyancy forces, we can show that $\frac{Ra}{Re^2 Pr} = 1$.

We first validate the code in a purely hydromagnetic flow, and in a second time, we solve a thermoconvective case to simulate the Rayleigh-Bénard instability. For both cases, we use analytical solutions.

2.1 Hartmann flow

We consider a 2D channel flow, similar to a Poiseuille flow, and we apply a constant vertical magnetic field $\mathbf{B_0}$ and a constant pressure gradient $-\frac{\partial p}{\partial x}$, as described in Fig. 1. In this configuration, an analytical solution is possible, assuming a steady unidimensional flow.

The steady equation of motion then becomes:

$$\nu \frac{\partial^2 u}{\partial z^2} = -\frac{1}{\rho_0}\frac{\partial p}{\partial x} + \frac{1}{\rho_0}\sigma B_0^2 u, \tag{5}$$

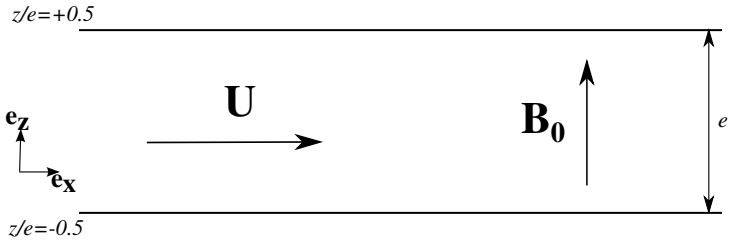

Figure 1: Hartmann flow.

where u is the horizontal component of $\mathbf{U}$ of the velocity. The solution is then:

$$u(z) = u_0 \left[1 - \frac{\cosh Ha(z/e)}{\cosh Ha/2} \right], \tag{6}$$

introducing the Hartmann number $Ha = B_0 e \sqrt{\frac{\sigma}{\rho_0 \nu}}$ and $u_0 = -\frac{1}{\sigma B_0^2} \frac{\partial p}{\partial x}$. Note that when $B_0 = 0$ we get the classical Poiseuille equations. The results are represented in Fig. 2, where a 64-point regular grid in the z direction was used. We have a good agreement with the theoritical profiles of the Hartmann, which constitutes the first step of the validation of our code.

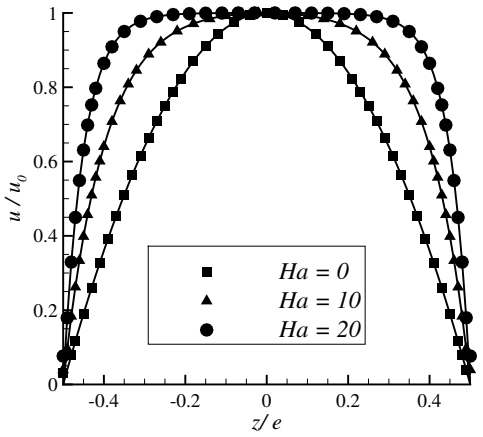

Figure 2: Velocity profiles obtained through Jadim computations of the Hartmann flow. The symbols stand for different Ha numbers and the solid lines represent the theoritical profiles. As Ha increases, the shear rate at the walls increases and the velocity profile is flattened.

2.2 Natural convection validation

We now need to validate the code in natural convection. For this purpose, we used a theorical solution proposed by Garandet et al. [7]. This case consists in a vertically differentially heated cavity at T_h and T_c (with $T_h > T_c$) and with an aspect ratio $L/e \gg 1$ as described in Fig. 3.

Far away from the walls, the flow can be considered horizontal and we have:

$$u(z) = u_0 \frac{Gr}{Ha^2} \left(\frac{\sinh(2Ha\, z/e)}{2\sinh(Ha)} - \frac{z}{e} \right), \tag{7}$$

where $u(z)$ is the horizontal component of the velocity, and u_0 is estimated using viscous eddies. Considering

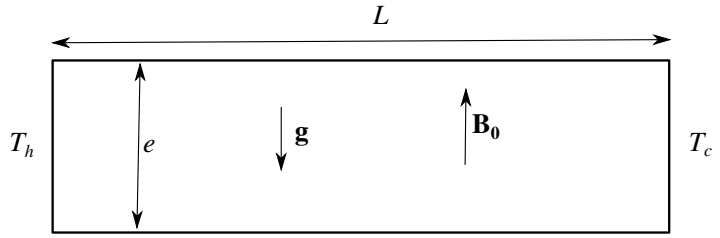

Figure 3: Rectangular cavity with vertically heated walls.

horizontal insulated walls, we also have the analytical non-dimensional temperature profile:

$$T(x,z) = \frac{ex}{L^2}\frac{PrGr(e/L)}{Ha^2}\left[\frac{1}{2Ha^2}\frac{\sinh(Haz/e)}{2\sinh(Ha/2)} - \frac{(z/e)^3}{6} + \left(\frac{1}{8} - \frac{\cosh(Ha/2)}{2Ha\sinh(Ha/2)}\right)\frac{z}{e}\right]. \tag{8}$$

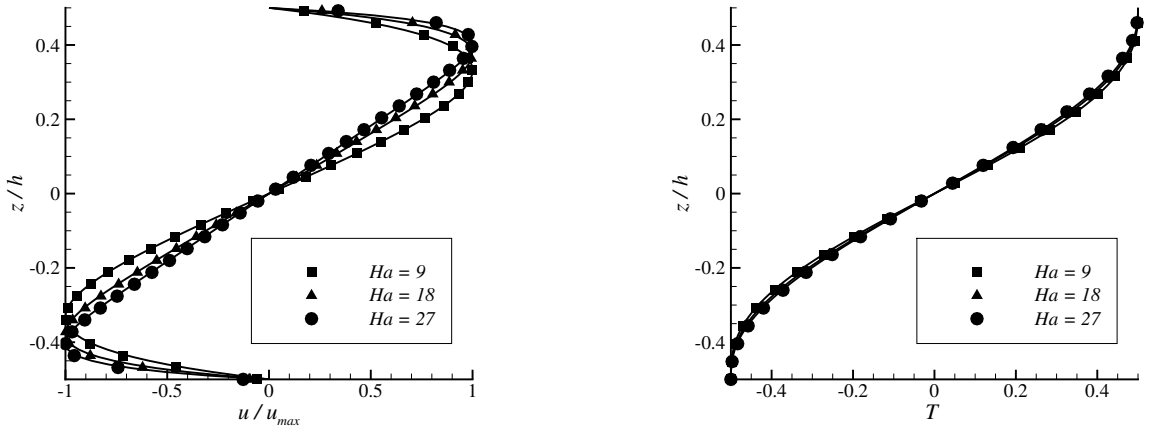

(a) Velocity profiles at the center of the cavity.

(b) Temperature profiles at the center of the cavity.

Figure 4: Jadim computations of natural convection between vertically heated plates. The symbols stand for different *Ha* numbers and the solid lines represent the analytical solutions from Garandet et al. [7].

We then have the velocity and temperature profiles in Fig. 4. The computations are in accordance with the analytical profile.

3 Three-dimensional simulation of Rayleigh-Bénard convection in presence of a magnetic field

In this case, we consider a cavity of aspect ratio $1 \times 10 \times 5$ and of height $e = 0.02m$, the computational grid is regularly spaced with a number of points $64 \times 256 \times 128$. The cavity is heated from below and cooled from above and vertical walls are insulated. Gravity is acting along the smallest side of the cavity. For the simulation, the properties of liquid Gallium were used, since it will be used to simulate molten steel at over 2500K. They are listed at table 1 and taken from Iida and Guthrie [8] and Okada and Ozoe [9].

3.1 Qualitative structure of the flow

At sufficiently high *Ra* numbers, results without magnetic field in Fig. 5(a) show that 3D effects are of importance. Indeed, non-linear effects (3D motion) appear right after the onset of convection. The magnetic field strongly

Property	Symbol	Units	Value
Density	ρ_0	$\mathrm{kg \cdot m^{-3}}$	6095
Thermal expansion coefficient	β	$\mathrm{K^{-1}}$	$1.27 \cdot 10^{-4}$
Kinematic viscosity	ν	$\mathrm{m^2 \cdot s^{-1}}$	$3.2 \cdot 10^{-7}$
Thermal diffusivity	κ	$\mathrm{m^2 \cdot s^{-1}}$	$1.27 \cdot 10^{-5}$
Thermal conductivity	k	$\mathrm{W \cdot m^{-1} \cdot K^{-1}}$	31
Electrical conductivity	σ	$\mathrm{S \cdot m^{-1}}$	$3.85 \cdot 10^6$

Table 1: Physical properties of liquid Gallium

affects the flow structure, as seen in Fig. 5(b). The three-dimensional patterns tend to be destructed, and two-dimensional convection rolls appear, which concurs with Burr and Müller [4]. One can also notice that the magnetic field are smooths the flow structures. This happens for the same reason that magnetic effects kill the isotropic character of turbulence [10]. We also see that the flow becomes 3D when the Ra is high enough, as it is shown in Fig. 5(c).

3.2 Heat transfer

Computations show that the magnetic field affects the flow dynamics. It affects as well the heat transfer. We define the local heat transfer coefficient at the walls, as well as its average (over the surface of the wall S):

$$h = \frac{k}{\Delta T}\frac{\partial T}{\partial z}\bigg|_{walls}, \tag{9}$$

$$\overline{h} = \frac{k}{\Delta T}\frac{1}{S}\iint \frac{\partial T}{\partial z}\bigg|_{walls} \mathrm{d}S, \tag{10}$$

where k is the thermal conductivity of the fluid and we consider the direction z to be normal to the horizontal walls. We also define the dimensionless heat transfer coefficients, the local and averaged Nusselt number:

$$Nu = \frac{he}{k}, \tag{11}$$

$$\overline{Nu} = \frac{\overline{h}e}{k}. \tag{12}$$

The results, presented in Fig. 6, show large variations of the Nusselt number at the horizontal walls both with and without magnetic field. But the presence of a magnetic field implies a different repartition of hot and cold spots. Figure 6 shows that the repartition of the regions where heat transfer is strong or low follows the same patterns as the convective structures. Due to convective motions, the local Nu can be lower than unity.

However, even if the surface averaged Nu at the walls is reduced in the presence of a magnetic field, it remains of the same order of magnitude, as shown in Fig. 7. The simulations at $Ha = 0$ are found to be in a good agreement with experimental results from Rossby [2], Aurnou and Olson [3]. The direction of the rolls is different without a magnetic field at low Ra and at a higher Ra and with a magnetic field. We suppose that this is due to confinement effects. The change in convection patterns is of importance in the case of corium-concrete interaction. In those experiments, the ablation rate of the concrete is proportional to the heat flux. Strong local variations of heat transfer due to the magnetic field will generate a wrong local ablation rate and question those experiments. Therefore, simulations of a case more representative of the corium-concrete interaction will be computed.

4 Stability analysis

In this section, we propose to investigate the linearised dynamic of the Rayleigh-Bénard flow subject to a constant magnetic field. We aim to compare the most unstable wavelength with the wavelength of the stationnary rolls obtained with Jadim at a Ra slightly above the critical Rayleigh number. To this end, we provide a finite difference scheme to solve the growth rate s of the Rayleigh-Bénard instability according to the wavenumber k, as an extent to Chandrasekhar's theory [1].

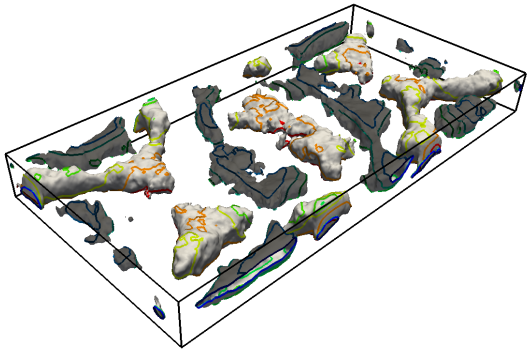

(a) $Ra = 5 \cdot 10^4$, $Ha = 0$.

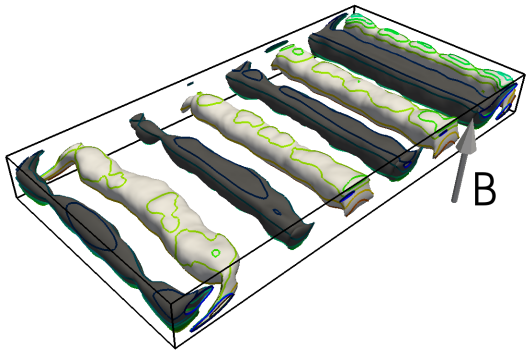

(b) $Ra = 5 \cdot 10^4$, $Ha = 18$, vertical magnetic field.

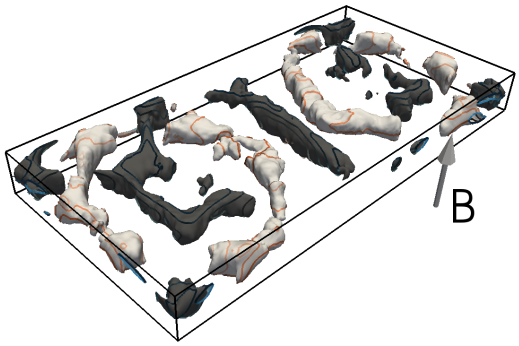

(c) $Ra = 1.5 \cdot 10^5$, $Ha = 18$, vertical magnetic field.

Figure 5: Surfaces of vertical isovelocity. Light grey represents ascending structures and dark grey represents descending structures . Colored lines represent isothermal contours.

4.1 Linearisation of the equations

Remembering from Ampère's law that $\mathbf{j} = \frac{1}{\mu_0}\nabla \times \mathbf{B}$, and hence we can rewrite the Lorentz force as $\mathbf{j} \times \mathbf{B} = \frac{1}{\mu_0}(\nabla \times \mathbf{B}) \times \mathbf{B} = \frac{1}{\mu_0}\left[(\mathbf{B} \cdot \nabla)\mathbf{B} - \nabla\frac{\mathbf{B^2}}{\mathbf{2}}\right]$. The last term $-\nabla\frac{\mathbf{B^2}}{\mathbf{2\mu_0}}$ can be combined with $-\nabla p$ and is thus called the magnetic pressure gradient. The momentum equation becomes:

$$\frac{\mathrm{D}\mathbf{U}}{\mathrm{D}t} = -\frac{1}{\rho_0}\nabla\left(p + \frac{\mathbf{B^2}}{\mathbf{2\mu_0}}\right) + \beta(T - T_0)\mathbf{g} + \nu\triangle\mathbf{U} + \frac{1}{\rho_0\mu_0}(\mathbf{B} \cdot \nabla)\mathbf{B}. \tag{13}$$

Accounting for the Joule dissipation in the heat equation reads:

$$\frac{\mathrm{D}T}{\mathrm{D}t} = \kappa\triangle T + \frac{1}{\rho c_p}\frac{j^2}{\sigma}, \tag{14}$$

where c_p is the specific heat. We shall see that the Joule dissipation will not be of importance, since it is a second order term. The last equation is the induction equation for the magnetic field $\mathbf{B}$, obtained from the Maxwell equations:

$$\frac{\partial\mathbf{B}}{\partial t} = \eta\nabla^2\mathbf{B} + \nabla \times (\mathbf{U} \times \mathbf{B}), \tag{15}$$

with $\eta = 1/\mu_0\sigma$ the magnetic diffusivity.

We consider the purely conductive and stable state that we infinitesimally perturbate. The velocity, temperature and magnetic fields become:

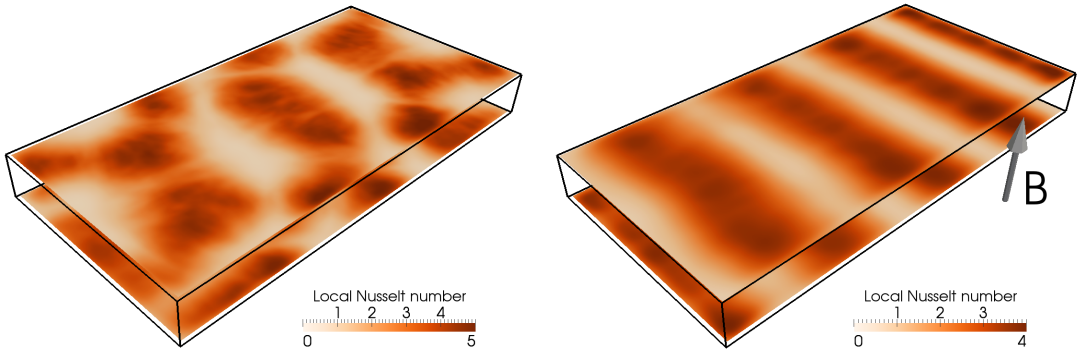

(a) $Ha = 0$. (b) $Ha = 18$, vertical magnetic field.

Figure 6: Local Nusselt number at the walls for $Ra = 5 \cdot 10^4$.

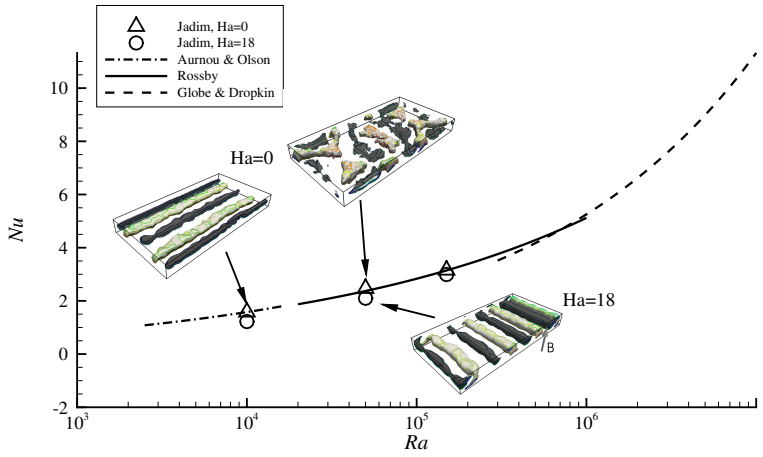

Figure 7: Comparison of Jadim simulations with experimental *Nu*-*Ra*-correlations. Symbols represent the simulations and the lines represent the experimental correlations of sevenral authors.

$$\mathbf{U} = \mathbf{U_0} + \mathbf{u}, \tag{16}$$
$$T = T_0(z) + \vartheta, \tag{17}$$
$$\mathbf{B} = \mathbf{B_0} + \mathbf{b}, \tag{18}$$

where $\mathbf{U_0}$, $T_0(z) = \Delta T \frac{z}{h}$ and $\mathbf{B_0} = \text{constant} \cdot \mathbf{e_z}$ are the stable fields, and $\mathbf{u}$, ϑ and $\mathbf{b}$ are the small perturbations. Note that since there is no movement, $\mathbf{U_0} = \mathbf{0}$. We now linearise the equations and we obtain:

$$\frac{\partial \triangle w}{\partial t} = g\beta\left(\frac{\partial^2 \vartheta}{\partial x^2} + \frac{\partial^2 \vartheta}{\partial y^2}\right) + \nu \triangle^2 w + \frac{B_0}{\rho \mu_0}\frac{\partial \triangle b_z}{\partial z}, \tag{19}$$
$$\frac{\partial \vartheta}{\partial t} = \kappa \triangle \vartheta + \frac{\Delta T}{h} w, \tag{20}$$
$$\frac{\partial b_z}{\partial t} = \eta \triangle b_z + B_0 \frac{\partial w}{\partial z}. \tag{21}$$

The equations (19) and (21) are the $\mathbf{e_z}$ component of rotationnal of vorticity equation and of the induction equation, w is the $\mathbf{e_z}$ component of the velocity. Using a characteristic viscous time, we get the non dimensional equations:

$$\frac{\partial \triangle^* w^*}{\partial t^*} = \frac{Ra}{Pr}\left(\frac{\partial^2 \vartheta^*}{\partial x^{*2}} + \frac{\partial^2 \vartheta}{\partial y^{*2}}\right) + \triangle^{*2} w^* + \frac{Ha^2}{Pm}\frac{\partial \triangle^* b_z^*}{\partial z^*}, \tag{22}$$

$$\frac{\partial \vartheta^*}{\partial t^*} = \frac{1}{Pr}\triangle^* \vartheta^* + w^*, \tag{23}$$

$$\frac{\partial b_z^*}{\partial t^*} = \frac{1}{Pm}\triangle^* b_z^* + \frac{\partial w^*}{\partial z^*}, \tag{24}$$

with $Pm = \mu_0 \sigma \nu$, the magnetic Prandtl number. We look for plane waves solutions:

$$\begin{pmatrix} w^* \\ \vartheta^* \\ b_z^* \end{pmatrix} = \begin{pmatrix} W(z) \\ \Theta(z) \\ \mathcal{B}(z) \end{pmatrix} \exp(\mathrm{i}(k_x x^* + k_y y^*) + s t^*). \tag{25}$$

W, Θ, $\mathcal{B}$ are the amplitudes of the perturbations, k_x and k_y are the dimensionless wavenumbers, and s is the growth rate of the instability. Chandrasekhar proposed to focus on the marginal stablity *i.e.* $s = 0$. He demonstrated the stabilising effect of the magnetic field on thermal convection (Fig. 8). If Ha increases, Ra_c and k_c (represented by the minimums of the curves in Fig. 8(a)) also inrease, and in the limit $Ha \longrightarrow \infty$, we have $Ra_c \longrightarrow \pi^2 Ha^2$, as we see in Fig. 8(b). In other words, if for a given Ha, the Ra number is below Ra_c, there is no convection, but only conduction.

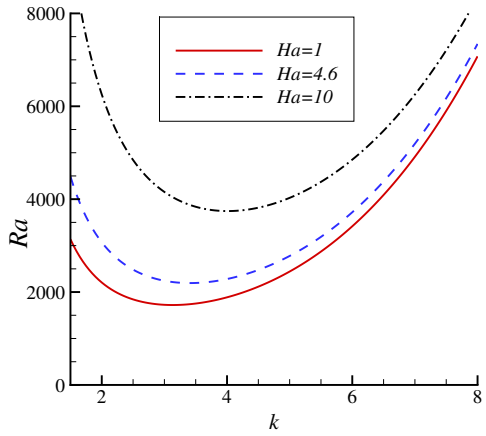

(a) The minimum of each curves represents the critical values of Ra and k. They are delayed to higher values when Ha increases.

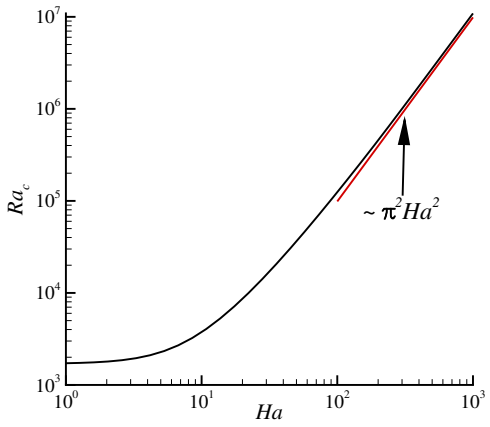

(b) There is destabilisation for Ra above the curve. Higher Ha imply higher critical Ra.

Figure 8: Linear stability analysis .

We propose to focus on what happens beyond $s = 0$, while staying in the linear domain. We use these solutions in equations (22)-(24), and we have the following system:

$$s(D^2 - k^2)W = -\frac{Ra}{Pr}k^2\Theta + (D^2 - k^2)^2 W + \frac{Ha^2}{Pm}[D(D^2 - k^2)\mathcal{B}], \tag{26}$$

$$s\Theta = \frac{1}{Pr}(D^2 - k^2)\Theta + W, \tag{27}$$

$$s\mathcal{B} = \frac{1}{Pm}(D^2 - k^2)\mathcal{B} + DW, \tag{28}$$

where $D = \dfrac{\partial}{\partial z^*}$ and $k^2 = k_x^2 + k_y^2$. We propose to solve this generalised eigenvalue problem with a finite difference scheme.

4.2 Finite difference scheme for the generalised eigenvalue problem

4.2.1 Numerical schemes

Let us consider the vector x that either stands for W, Θ, or $\mathcal{B}$ and we discretise in the z direction and for a number of points Nz, the space step is $\Delta z = \frac{1}{Nz}$. We choose the following second order schemes to approximate the derivatives:

$$x_i' = \frac{x_{i+1} - x_{i-1}}{2\Delta z} \tag{29}$$

$$x_i'' = \frac{x_{i+1} + x_{i-1} - 2x_i}{\Delta z^2} \tag{30}$$

$$x_i''' = \frac{x_{i+2} - x_{i-2} - 2x_{i+1} + 2x_{i-1}}{2\Delta z^3} \tag{31}$$

$$x_i^{(4)} = \frac{x_{i+2} + x_{i-2} - 4x_{i+1} - 4x_{i-1} + 6x_i}{\Delta z^4} \tag{32}$$

Let us express the problem as a generalised eigenvalue problem:

$$sA\mathbf{X} = B\mathbf{X}, \tag{33}$$

where:

$$\mathbf{X} = \begin{pmatrix} W_0 \\ \vdots \\ W_{Nz} \\ \Theta_0 \\ \vdots \\ \Theta_{Nz} \\ \mathcal{B}_0 \\ \vdots \\ \mathcal{B}_{Nz} \end{pmatrix}, \; A = \begin{pmatrix} A_{11} & A_{12} & A_{13} \\ A_{21} & A_{22} & A_{23} \\ A_{31} & A_{32} & A_{33} \end{pmatrix}, \; B = \begin{pmatrix} B_{11} & B_{12} & B_{13} \\ B_{21} & B_{22} & B_{23} \\ B_{31} & B_{32} & B_{33} \end{pmatrix}, \tag{34}$$

and the A_{ij}, B_{ij} are $Nz \times Nz$ matrices, s is the eigenvalue of the problem. As shown in the following paragraph, the matrices A and B depend on Ra, Ha, Pr, Pm and k. For a given value of k, we solve the eigenvalue problem to obtain s and the profiles of the perturbation amplitudes (the eigenvector $\mathbf{X}$).

4.2.2 Expression of the matrices

We can note that the matrices A_{ij} and B_{ij} will be $(n+1)$-diagonal where n is the order of derivation. Replacing the terms in equations (26)-(28) with the expressions given by (29)-(32):

$$A_{11} = \frac{1}{\Delta z^2} \begin{pmatrix} a_{11}^{11} & a_{11}^{12} & 0 & \cdots & 0 \\ 1 & -2 & 1 & \ddots & \vdots \\ 0 & \ddots & \ddots & \ddots & 0 \\ \vdots & \ddots & 1 & -2 & 1 \\ 0 & \cdots & 0 & a_{11}^{Nz,Nz-1} & a_{11}^{Nz,Nz} \end{pmatrix}, \; A_{22} = A_{33} = \mathbb{I}, \; A_{ij,i\neq j} = 0, \tag{35}$$

where $\mathbb{I}$ is the identity matrix. Ther terms a_{11}^{11}, a_{11}^{12}, $a_{11}^{Nz,Nz-1}$ and $a_{11}^{Nz,Nz}$ will be given by the boundary conditions. Those matrices represent the terms on the left side of the equations, and except for A_{11}, there is no derivative term which implies the matrices to be diagonal. The B_{ij} matrices represent the coupling between the different equations. Let $b_{ij}^{(0)}$, $b_{ij}^{(-1)}$, $b_{ij}^{(-2)}$, $b_{ij}^{(+1)}$, $b_{ij}^{(+2)}$ be the main, first lower, second lower, first upper and second upper diagonal terms

of the matrix. The inner aspect of the matrix is:

$$B_{ij} = \begin{pmatrix} \ddots & \ddots & \ddots & \ddots & \ddots & & \\ & b_{ij}^{(-2)} & b_{ij}^{(-1)} & b_{ij}^{(0)} & b_{ij}^{(+1)} & b_{ij}^{(+2)} & \\ & & \ddots & \ddots & \ddots & \ddots & \ddots \end{pmatrix}. \tag{36}$$

The other terms are all equal to zero. The two first and the two last lines will be given by the boundary conditions. We can first express the B_{11}, B_{22}, B_{33} matrices. The B_{11} matrix is pentadiagonal and we have:

$$b_{11}^{(0)} = \frac{6}{\Delta z^4} + 4\frac{k^2}{\Delta z^2} + k^4, \tag{37}$$

$$b_{11}^{(+1)} = b_{11}^{(-1)} = -\frac{4}{\Delta z^4} - \frac{2k^2}{\Delta z^2}, \tag{38}$$

$$b_{11}^{(+2)} = b_{11}^{(-2)} = \frac{1}{\Delta z^4}. \tag{39}$$

The B_{22} et B_{33} matrices are tridiagonal, hence $b_{22}^{(+2)} = b_{22}^{(-2)} = b_{33}^{(+2)} = b_{33}^{(-2)} = 0$. We can express the other terms as:

$$b_{22}^{(0)} = -\frac{1}{Pr}\frac{k^2+2}{\Delta z^2}, \tag{40}$$

$$b_{22}^{(+1)} = b_{22}^{(+1)} = \frac{1}{Pr}\frac{1}{\Delta z^2}, \tag{41}$$

$$b_{33}^{(0)} = -\frac{1}{Pm}\frac{k^2+2}{\Delta z^2}, \tag{42}$$

$$b_{33}^{(+1)} = b_{33}^{(+1)} = \frac{1}{Pm}\frac{1}{\Delta z^2}. \tag{43}$$

The B_{13} and B_{31} are also pentadiagonal and tridiagonal matrices and the diagonal terms can be expressed as:

$$b_{13}^{(0)} = 0, \tag{44}$$

$$b_{13}^{(+1)} = -b_{13}^{(-1)} = \frac{Ha^2}{Pm}\left(\frac{1}{\Delta z^3} + \frac{k^2}{2\Delta z}\right), \tag{45}$$

$$b_{13}^{(+2)} = b_{13}^{(-2)} = \frac{1}{2\Delta z^3}, \tag{46}$$

$$b_{31}^{(0)} = 0, \tag{47}$$

$$b_{31}^{(+1)} = -b_{31}^{(-1)} = \frac{1}{2\Delta z}. \tag{48}$$

Since the magnetic field and the temperature do not influence each other, the B_{23} and B_{32} are empty. If we took in consideration the Joule dissipation, the B_{32} would not be zero, but since the equations were linearised and the Joule dissipation is a second order term, it does not appear here. B_{12} and B_{21} are diagonal matrices and express as:

$$B_{12} = -\frac{Ra}{Pr}k^2\mathbb{I}, \qquad B_{21} = \mathbb{I}. \tag{49}$$

4.2.3 Boundary conditions

We have not discussed the boundary conditions so far. At the walls, the velocity is zero due to the non-slip condition and we suppose that walls are maintained at constant temperature, so the temperature perturbation is also zero. This follows:

$$W_0 = W_{Nz} = 0, \qquad \Theta_0 = \Theta_{Nz} = 0. \tag{50}$$

However, for the magnetic field, the boundary condition depends on the electrical properties of the wall. Assuming a perfectly conductive wall, the perturbation is zero at the walls (Dirichlet's conditions at the walls, $\mathcal{B} = 0$).

4.2.4 Marginal stability

In this part, we look for the wavenumber $k = k_c$ such that the maximum of the real part of s is zero. We compare the critical values of the Rayleigh number Ra_c and of the wavenumber k_c with those given by the linear stability theory from Chandrasekhar [1].

The classic linear stability theory gives the values of Ra_c and k_c for the onset of convection. For $B_0 = 0$, the critical values for the Rayleigh number and the wavenumber of $Ra_c = 1708$ and $k_c = 3.11$. Using a number of points $N_z = 256$, we find with the finite difference scheme that $Ra_c = 1734$ and $k_c = 3.14$. The results presented in Fig. 9(a) were obtained with seven different Hartmann numbers that are evenly spaced on the logarithmic scale between $Ha = 1$ and $Ha = 21.5$. Figure 9(b) shows a relative error ε_{Ra} of the order of 2% for the critical Rayleigh number and the relative ε_k error for the critical wavenumber less than 1%.

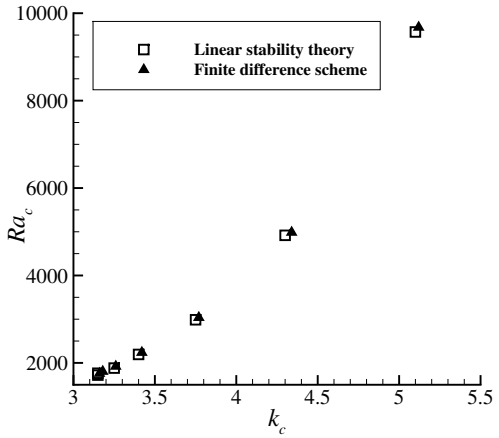

(a) Comparison of the linear stability theory and the finite difference scheme.

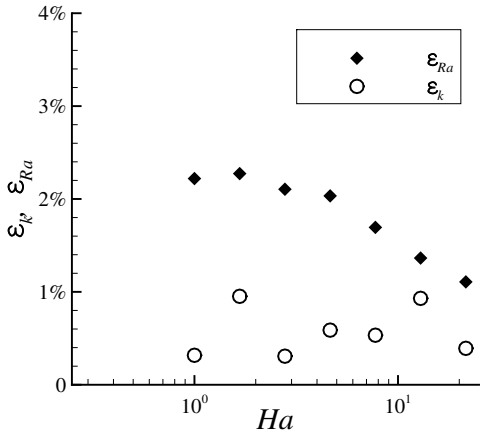

(b) Relative error to the theorical k_c and Ra_c.

Figure 9: Marginal stability to the finite difference scheme.

4.2.5 Eigenvectors and growth rate of the instability

Thanks to this finite difference scheme, we can access the eigenfunctions of temperature, velocity and magnetic field perturbations. The growth rate is given by the maximal value of the real part of s. The results are shown in Fig. 10 for $Ha = 0$ and in Fig. 11 for $Ha = 10$. Figures 10(a) and 11(a) show that the magnetic field enlarges the critical wavenumber k_c. The amplitudes of the pertubations for $k = k_c$ along the z axis are the eigenvectors for this given k and are shown in Figs. 10(b) and 11(b). However, the eigenvectors remain relatively close. We can nevertheless notice that the amplitude of the perturbations for Θ is slightly lower whith an impressed magnetic field. Figure 11(b) shows that the amplitude of the perturbation of $\mathcal{B}$ is antisymmetric, which contrasts with the other amplitudes that are symmetric.

We can see that the perturbation are zero at the walls, as imposed by the boundary conditions, as well as the $DW = 0$.

5 Conclusion and perspectives

The simulations confirm that three dimensional effects are of importance and the flow cannot be considered as 2D. However, as magnetic effects become significant enough, we observe that the flow becomes two-dimensional again. This change in the flow structure is essential and modifies the local heat transfer, but the global heat transfer remains of the same order of magnitude. Simulations in a more realistic case of a corium-concrete interaction will be computed, in order to see if the local variations of heat transfer are of importance when the pool is subjected to a steady magnetic field. Next steps of this work will focus on a time-varying magnetic field, in order to study the

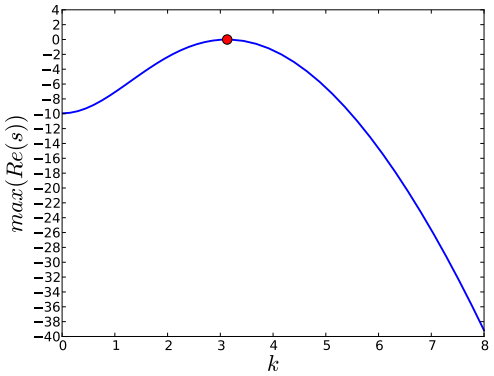

(a) Growth rate ($\sim max(Re(s))$) depending on k. The red dot represents the $k_c = 3.14$ where $max(Re(s)) = 0$.

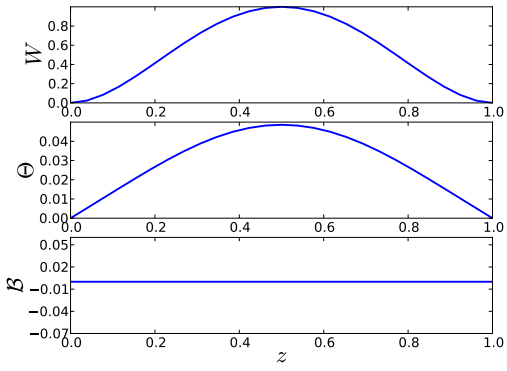

(b) Eigenvectors for $k = k_c = 3.14$.

Figure 10: Eigenvectors and growth rate for $Ra = 1734 \sim Ra_c$ and $Ha = 0$.

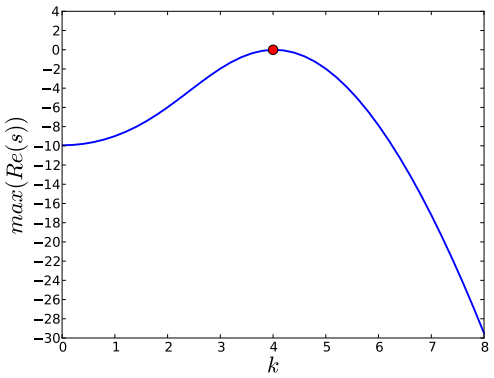

(a) Growth rate ($\sim max(Re(s))$) depending on k. The red dot represents the $k_c = 4.0$ where $max(Re(s)) = 0$.

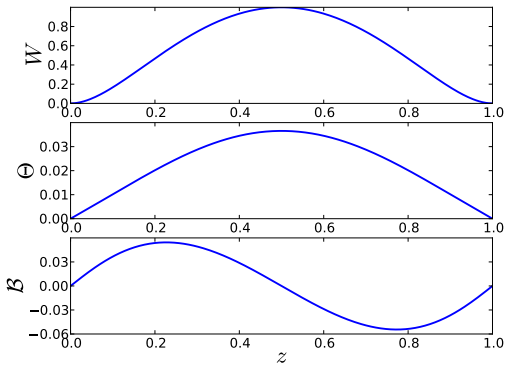

(b) Eigenvectors for $k = k_c = 4.0$.

Figure 11: Eigenvectors and growth rate for $Ra = 3800 \sim Ra_c$ and $Ha = 10$.

influence of Faraday's induction on the flow dynamic. It will also allow us to design an experimental test rig to confirm the accuracy of the simulations.

The linear stability analysis seems promising and the next developments will focus on including a time-varying **B**, to show how a sinusoidal magnetic field affects the onset of convection.

References

[1] S. Chandrasekhar. *Hydrodynamic and hydromagnetic stability*. Dover Publications, Inc, 1981.

[2] H. T. Rossby. A study of Bénard convection with and without rotation. *Journal of Fluid Mechanics*, 36: 309–335, 4 1969.

[3] J.M. Aurnou and P.L. Olson. Experiments on Rayleigh–Bénard convection, magnetoconvection and rotating magnetoconvection in liquid gallium. *Journal of Fluid Mechanics*, 430:283–307, 2001.

[4] U. Burr and U. Müller. Rayleigh–Bénard convection in liquid metal layers under the influence of a vertical magnetic field. *Physics of Fluids*, 13(11):3247–3257, 2001.

[5] U. Burr and U. Müller. Rayleigh–Bénard convection in liquid metal layers under the influence of a horizontal magnetic field. *Journal of Fluid Mechanics*, 453:345–369, 2002.

[6] S. Globe and D. Dropkin. Natural convection heat transfer in liquids confined by two horizontal plates and heated from below. *J. Heat Transfer*, 81(1):24–28, 1959.

[7] J.P. Garandet, T. Alboussiere, and R. Moreau. Buoyancy driven convection in a rectangular enclosure with a transverse magnetic field. *International Journal of Heat and Mass Transfer*, 35(4):741–748, 1992.

[8] T. Iida and R. Guthrie. The physical properties of liquid metals. *Clarendon Press*, 1988.

[9] K. Okada and H. Ozoe. Experimental heat transfer rates of natural convection of molten gallium suppressed under an external magnetic field in either the x, y, or z direction. *Journal of Heat Transfer*, 114(1):107–114, 1992.

[10] J. Sommeria and R. Moreau. Why, how, and when, MHD turbulence becomes two-dimensional. *Journal of Fluid Mechanics*, 118:507–518, 1982.